Supporting Information for "The Cluster Virtual Observatory for ULF Waves"

O.D. Constantinescu[1,2], K.H. Fornaçon[1], U. Motschmann[3], K.H. Glassmeier[1], I. Richter[1], F. Plaschke[1]

[1]Institute for Geophysics and Extraterrestrial Physics, TU Braunschweig, Germany

[2]Institute for Space Sciences, Bucharest, Romania

[3]Institute for Theoretical Physics, TU Braunschweig, Germany

Contents of this file

Introduction

This supplementary material describes the data and the plots available from the online Cluster Virtual Observatory for ULF waves. For a description of the data processing please see section 4.1.1 of the main paper.

Description of the tables listing available ULF parameters

All the wave parameters stored in the CVO database are listed in the tables Tab. S1 and Tab. S2.

The column "input" shows which data was used to compute the parameter (the magnetic field, $\boldsymbol{B}$, the electric field, $\boldsymbol{E}$, and/or the particle density, n).

The name of the parameter is shown in the column "parameter". Here, RH stands for Right Hand, LH for Left Hand, PSD for Power Spectral Density, $\boldsymbol{k}$ for the wave vector, LMC for the Local Magnetic Coordinates system described below, and $\boldsymbol{e}$ for the unit vectors. The LMC is defined starting from the position vector of the spacecraft in the Solar Magnetic (SM) coordinate system (Laundal & Richmond, 2017): The z axis is defined as the geocentric radial direction, the y axis is defined by the cross product of the z axis of the SM coordinate system and the radial direction: $\hat{\boldsymbol{e}}'_y = \hat{\boldsymbol{e}}_z^{\mathrm{SM}} \times \hat{\boldsymbol{e}}'_z / |\hat{\boldsymbol{e}}_z^{\mathrm{SM}} \times \hat{\boldsymbol{e}}'_z|$. This axis points eastward in the toroidal direction. The x axis completes the right handed system and points southward in the poloidal direction: $\hat{\boldsymbol{e}}'_x = \hat{\boldsymbol{e}}'_y \times \hat{\boldsymbol{e}}'_z$. The LMC system is useful in the inner magnetosphere where the dipole field dominates.

The formula used to compute the parameter is shown in the column "expression". The duration of the window used for computing the parameters is $W = N\mathrm{d}t$, with $N = 2048$ samples and $\mathrm{d}t = 1\,\mathrm{s}$. The rest of the symbols are defined in the main paper (refer to the next column, "Eq.").

The name of the file containing the parameter is shown in the last column. The full url to the file is: `http://plasma.spacescience.ro/waves/spectra-data/Fourier/CN/YYYY/FileName/FileName_YYYY-MM-DD.hdf`. This path can be used for direct access to download multiple files if desired.

Description of the wave vector direction set

The first panel (a) and the last two panels (g,h) in this set, illustrated in Fig. S1 for Cluster 1 on 2005.05.20, are the same as the corresponding ones in the *Basic parameters* set illustrated in the main paper Fig. 1 discussed in sec. 4.1.2. Panel (b) shows the PSD of the coherent part of the fluctuations computed from the coherent intensity Eq. (15): $\rho_{\mathrm{coh}} = 2WI_{\mathrm{coh}}$.

The two panels in the third row (c,d) show the direction of the wave vector as scatter plots in the (θ, φ) domain. The time is colour coded. The directions corresponding to 30° cones around the positive and the negative directions of the coordinate system axes are plotted as ellipses for the x and y axes and as horizontal lines for the z axis. The coordinate system used for the left hand side panel (c) is the LMC defined above. The right hand side panel (d) uses the GSE coordinate system with the x axis pointed towards the Sun and the y axis in the ecliptic plane. On this day, the propagation direction is not well defined in front of the bowshock which is crossed around 06:00 (black and cyan colours). Inside the bowshock it seems that the waves prefer to propagate in the poloidal direction, with a westward additional component close to the bowshock, which switches to an eastward component towards the end of the interval. Together with the position in the dayside magnetosheath, this suggests that in this case the waves propagate more along the magnetosheath than in the cross-magnetosheath direction. Considering the (anti)parallel to the magnetic field propagation evident in the panel (g) of Fig. 1 in the main paper, this reflects the draping of the magnetic field lines around the magnetopause. As discussed in Sec. 2 of the main paper, there is a sign ambiguity in the determination of the wave vector, i.e. the waves might in fact propagate in the opposite direction. This gives us the freedom to chose the sign of the wave vector such as to correspond to RH polarized waves with respect to the propagation direction.

The next two panels (e,f) show the orientation of the wave vector $\boldsymbol{k}$ as given by the φ angle made with the meridional plane and by the θ angle made with the radial direction in the LMC system. The corresponding frequencies are colour coded. This representation makes it possible to compare the wave vector direction with the mean magnetic field direction at different frequencies. In both panels the mean

0148-0227/23/$9.00

magnetic field direction is represented with a thick grey line in the background. The thick magenta line in the background marks the direction anti-parallel to the mean magnetic field. Since the sign of the determined wave vector is chosen by the convention above, in panel (e) we changed the ϕ angle to correspond to inward propagation ($|\theta| \geq 90$). The ϕ angle in this panel does not necessarily correspond to the wave vector direction in panels (c,d). The change from parallel to anti-parallel propagation observed around 16:00 reflects therefore the geometry of the magnetic field and not an abrupt change in the wave propagation direction.

Description of the B MFA set

Mean Field Aligned (MFA) related parameters are shown in Fig. S2. The top panel (a) is similar to the top panels from the previous discussed plot sets but now the magnetic field time series are represented in the MFA coordinate system. This system has the z axis aligned with the mean magnetic field vector. The mean magnetic field vector is computed using a boxcar average with the width equal to the sliding step $W/8 = 256\,\mathrm{s}$ used to compute the PSD. The y axis is orthogonal to the mean magnetic field - position vector plane: $\hat{\boldsymbol{e}}_y^{\mathrm{MFA}} = \hat{\boldsymbol{e}}_r^{\mathrm{GSE}} \times \hat{\boldsymbol{e}}_z^{\mathrm{MFA}} / |\hat{\boldsymbol{e}}_r^{\mathrm{GSE}} \times \hat{\boldsymbol{e}}_z^{\mathrm{MFA}}|$ and points roughly in the westward azimuthal direction in the inner magnetosphere. The x axis completes the right-handed system: $\hat{\boldsymbol{e}}_x^{\mathrm{MFA}} = \hat{\boldsymbol{e}}_y^{\mathrm{MFA}} \times \hat{\boldsymbol{e}}_z^{\mathrm{MFA}}$, roughly radial in the inner magnetosphere. The x and y directions can substantially deviate from the azimuthal and radial directions in the vicinity of the cusp regions and outside the dipolar field and they take more or less arbitrary directions outside the magnetosphere and in disturbed regions.

The three panels below the time series panel (b,c,d) show the power spectral densities for the three components of the magnetic field in the MFA system. In our case, x and y (radial and azimuthal) directions concentrate most of the wave energy, while little energy is contained in the fluctuations parallel to the mean magnetic field. This is made more obvious by the next panel (e) which illustrates the ratio between the power associated with the oscillations transversal to the magnetic field and the total wave power $(1 - C)$ Eq. (19). Most of the magnetic field fluctuations are clearly perpendicular, with the exception of some low frequency fluctuations close to the bowshock crossings and of the waves around 04 UT.

Though the parameters shown in the last three panels are not directly related to the MFA coordinate system, we chose to include them in this set to aid the analysis of the waves. The wave normal angle (g) and the ellipticity (h) were discussed before. When the noise contribution is isotropic, the coherence Eq. (14) shown in panel (f) is equivalent with the polarization degree Eq. (12) (Jones, 1979).

Description of the B – density set

This set, illustrated in Fig. S3, shows the parameters related to the electron density fluctuations. Because of time resolution and data availability restrictions of the particle instruments we derive the electron density from the spacecraft potential using the relations provided by Lybekk et al. (2012). The exact parameters used to derive the electron density were only determined up to 2010. From 2010 on we use the 2010 parameters. This means that the estimated electron density can deviate from the real one. However, the most important density related parameters, the coherence and the phase difference between the magnetic field and density fluctuations are independent on possible offset or scaling errors in the density. Therefore these parameters are also reliable after 2010. The co- and quad-spectrum values are affected by these errors, but they still describe qualitatively the relation between the magnetic field and the density.

The black line in the top panel (a) shows the magnetic field magnitude smoothed using a sliding window of 1024 s. The red line shows the density. Panel (b) shows the PSD of the magnetic field magnitude oscillations. The yellow line represents the electron density in logarithmic scale. The power spectral density of the density fluctuations is shown in panel (c).

The coherency between the magnetic field fluctuations and the density fluctuations, γ_{Bn} computed from Eq. (14) is plotted in panel (d) with power and polarization masks applied. The coherency is mostly low inside the magnetosheath, but somewhat larger in front of the magnetosheath. Even for these relatively low values, there is still coherent interaction between the field and the particles as reflected by the magnetic field - density phase differences plotted in the panel (e) below. The colours are assigned to the phase difference $\Delta\varphi_{Bn} = \varphi_B - \varphi_n$ as follows: red for opposite phase $(-180,^\circ -135^\circ)$ and $(135^\circ, 180^\circ)$, blue for in phase oscillations $(-45^\circ, 45^\circ)$, yellow for retarded magnetic field oscillations $(45^\circ, 135^\circ)$, and green for retarded density oscillations $(-135^\circ, -45^\circ)$. In addition to the power and polarization masks, a mask for coherency $\gamma_{Bn} < 0.5$ was applied. The larger coherency in front of the magnetosheath is reflected in much more stable phase differences across the time-frequency domain as inside the magnetosheath. Here, the field oscillates in opposition to the density, indicating consistent coupling between field and particles. Inside the high polarization time-frequency domains in the magnetosheath, the density fluctuations seem to be retarded from the magnetic field fluctuations, suggesting that the magnetic field drives the density and not the other way around.

The last three panels (f,g,h) in this set are the same as those in the *basic parameters* set in Fig. 1.

Description of the Poynting vector direction set

This set, illustrated in Fig. S4, aims to show the direction in which the waves energy flows. The magnetic field time series in the first panel (a) is the same as in Fig. 1. The next panel (b) shows the magnitude of the Poynting vector Eq. (23), with no mask applied. The electric field measured by the Electric Field and Wave Experiment (EFW) (Gustafsson et al., 1997) is downloaded from the CSA at a resolution of 25 vectors per second when available, otherwise a much lower resolution of one vector each 4 s is used. One should consider the caveats of the electric field instrument before interpreting these plots. For instance since the end of 2001 only three probes are functional on Cluster 1, same applies to Cluster 3 after mid 2002, and to Cluster 2 after mid 2007. The $\boldsymbol{v} \times \boldsymbol{B}$ electric field is removed and no field-aligned electric field is allowed.

The four panels below (c,d,e,f), showing the direction of the Poynting vector, are similar, and use the same coordinate system as for the wave vector direction in Fig. S1. However, in contrast with the wave vector direction, no sign uncertainty exists, and the Poynting vector direction is much more confined indicating a clear anti-sunward flow of the energy in the GSE (θ, φ) right hand side plot (c) and a westward toroidal flow in the left hand side plot (d). Remarkably, the energy flows in this direction during the entire day, despite increasing distance to the equatorial plane. Data points with the Poynting vector magnitude below $0.5\,\mu\mathrm{W\,km^{-2}\,Hz^{-1}}$ were discarded, and power and polarization masks were applied.

Panel (g) shows the angle between the Poynting vector and the mean magnetic field in the time-frequency domain. Inside the magnetosheath the Poynting vector direction changes from anti-parallel near the bowshock to parallel towards the end of the interval. This reflects the change in the background magnetic field orientation rather than a change in the Poynting vector direction, as evident from panel (e).

Description of the Poynting vector MFA set

The first two panels (a,b) of this last set of plots shown in Fig. S5, are the same as the first two panels in Fig. S1, and the last panel (h) is the same as panel (g) in Fig. S4. The remaining panels show the total power spectral density of the electric field (c), the components of the Poynting vector in the mean field aligned system defined for the *B MFA* plot set (c,d,e), and the angle between the wave vector and the Poynting vector, reduced to $(0°, 90°)$ due to the wave vector sign uncertainty (f).

Description of the yearly, monthly and daily configuration plots

Yearly overview plots for the entire mission duration are provided, an example being shown in Fig. S6. These are similar to the four years plots but are separated on months and in addition the trajectories in the (e,p) domain are also plotted inside the right hand side colour keys.

A more detailed view of the tetrahedron configuration is offered by the monthly plots. The plot for January 2005 is shown in Fig. S7. The projections of the orbit of the formation barycentre on the three GSE planes allow for a quick estimation of the tetrahedron shape for different magnetospheric regions, while the size of the tetrahedron together with the corresponding colour encoded shape is shown in the fourth panel. To aid linking of the line colour with the (e,p) space and to give a better overview of which regions of the (e,p) space are being visited during the month, the trajectory in the shape space is plotted in white in the colour-key.

The most detailed view of the configuration parameters is given by the daily plots. Fig. S8 is an example for 1st of January 2005. To give an overview of the magnetic field measurements the top panel shows the magnetic field magnitudes measured by the four spacecraft (C1 - black, C2 - red, C3 - green, C4 - blue). The magnetospheric regions in which each spacecraft finds itself are represented by the coloured bars at the bottom of the panel. Top bar for C1, bottom bar for C4. The magnetospheric regions are determined from the Goddard SSCWeb interface `http://sscweb.gsfc.nasa.gov` using IGRF internal and Tsyganenko 89C external model. The six inter-spacecraft distances are presented in the next panel, followed by the geocentric distances for all spacecraft an for the barycentre of the formation. The fourth panel shows the degeneration degree, defined as the radial coordinate in the (e, p) domain: $0 \leq \sqrt{e^2 + p^2} \leq \sqrt{2}$. A small degeneration indicates a near regular tetrahedron. The degeneration increases as the tetrahedron departs from the regular shape. The bottom left plot shows the trajectory in the (e,p) domain with the time colour coded. The projections of the orbit on the GSE (x,y), (x,z), and (y,z) planes and the geocentric distance of the barycentre are shown in the four bottom right plots.

References

Arthur, C. W., McPherron, R. L., & Means, J. D. (1976). A comparative study of three techniques for using the spectral matrix in wave analysis. *Radio Science*, *11*(10), 833–845. doi: 10.1029/RS011i010p00833

Fowler, R., Kotick, B., & Elliott, R. (1967). Polarization Analysis of Natural and Artificially Induced Geomagnetic Micropulsations. *J. Geophys. Res.*, *72*, 2871-2883. doi: 10.1029/JZ072i011p02871

Gustafsson, G., Bostrom, R., Holback, B., Holmgren, G., Lundgren, A., Stasiewicz, K., … Wygant, J. (1997, January). The Electric Field and Wave Experiment for the Cluster Mission. *Space Science Reviews*, *79*, 137-156. doi: 10.1023/A:1004975108657

Jones, A. (1979). On the Difference Between Polarisation and Coherence. *Journal of Geophysics*, *45*, 223-229.

Kodera, K., Gendrin, R., & de Villedary, C. (1977, Mar). Complex representation of a polarized signal and its application to the analysis of ULF waves. *J. Geophys. Res.*, *82*(7), 1245. doi: 10.1029/JA082i007p01245

Laundal, K. M., & Richmond, A. D. (2017, March). Magnetic Coordinate Systems. *Space Sci. Rev.*, *206*(1-4), 27-59. doi: 10.1007/s11214-016-0275-y

Lybekk, B., Pedersen, A., Haaland, S., Svenes, K., Fazakerley, A. N., Masson, A., … Trotignon, J.-G. (2012, January). Solar cycle variations of the Cluster spacecraft potential and its use for electron density estimations. *Journal of Geophysical Research (Space Physics)*, *117*, A01217. doi: 10.1029/2011JA016969

McPherron, R. L., Russell, C. T., & Coleman, P. J., Jr. (1972, July). Fluctuating Magnetic Fields in the Magnetosphere. II: ULF Waves. *Space Sci. Rev.*, *13*, 411-454. doi: 10.1007/BF00219165

Rankin, D., & Kurtz, R. (1970, Oct). Statistical study of micropulsation polarizations. *J. Geophys. Res.*, *75*(28), 5444-5458. doi: 10.1029/JA075i028p05444

Song, P., & Russell, C. T. (1999, January). Time Series Data Analyses in Space Physics. *Space Sci. Rev.*, *87*, 387-463. doi: 10.1023/A:1005035800454

Table S1. Parameters derived from a single quantity ($\boldsymbol{B}$, $\boldsymbol{E}$, or n)

input	parameter	unit	expression	Eq.	reference	file name
$\boldsymbol{B}$	Coherent power	$\mathrm{nT^2\,Hz^{-1}}$	$2W(\lambda'_1+\lambda'_2-2\lambda'_3)$	(15)	Song & Russell (1999)	`coh_power`
	PSD of $B_{j\mathrm{GSE}}$	$\mathrm{nT^2\,Hz^{-1}}$	$2W\lvert\tilde{B}_j\rvert^2$	(1)		`B_spec_xGSE`
						`B_spec_yGSE`
						`B_spec_zGSE`
	PSD of $B_{j\mathrm{MFA}}$	$\mathrm{nT^2\,Hz^{-1}}$	$2W\lvert\tilde{B}_j\rvert^2$			`B_spec_parallelMFA`
						`B_spec_perpMFA`
						`B_spec_azimuthalMFA`
						`B_spec_radialMFA`
	PSD of $\lvert\boldsymbol{B}\rvert$	$\mathrm{nT^2\,Hz^{-1}}$	$2W\lvert\widetilde{\boldsymbol{B}\rvert}$			`B_spec_abs`
	RH pol PSD	$\mathrm{nT^2\,Hz^{-1}}$	$2WA_+^2$	(16)	Kodera et al. (1977)	`power_right`
	LH pol PSD	$\mathrm{nT^2\,Hz^{-1}}$	$2WA_-^2$			`power_left`
	Linear pol PSD	$\mathrm{nT^2\,Hz^{-1}}$	$4WA_+A_-$	(17)		`power_lin`
	Circular pol PSD	$\mathrm{nT^2\,Hz^{-1}}$	$2W\lvert A_+^2-A_-^2\rvert$	(18)		`power_circ`
	Coherency of $\boldsymbol{B}$	–	$\lvert I_{xy}\rvert^2/(I_{xx}I_{yy})$	(14)	Rankin & Kurtz (1970)	`coherence`
	Polarization degree	–	$1-4\det(\mathcal{I})/\operatorname{Tr}(\mathcal{I})^2$	(12)	Fowler et al. (1967)	`polarization`
	Ellipticity	–		(13)	Arthur et al. (1976)	`ellipticity`
	Transv. power ratio	–	$\rho_{\mathrm{transversal}}/\rho_{\mathrm{total}}$	(19)		`compr_ratio`
	Eigenvalues	$\mathrm{nT^2}$	λ'_j			`eigen_vals0`
						`eigen_vals1`
						`eigen_vals2`
	Eigenvalues ratio	–	$\lambda'_{\mathrm{intermediate}}/\lambda'_{\mathrm{minim}}$			`ev_ratio`
	$\boldsymbol{k}$ direction in GSE	deg	eigenvector $\boldsymbol{v}'_3$	(10)	McPherron et al. (1972)	`k_theta_gse`
						`k_phi_gse`
	$\boldsymbol{k}-\boldsymbol{B}$ angle	deg	$\arccos(\boldsymbol{k}\cdot\boldsymbol{B})$			`kb_angle`
	$\boldsymbol{k}-\boldsymbol{e}_{j\mathrm{LMC}}$ angle	deg	$\arccos(k_{j\mathrm{LMC}})$			`alpha_k_radSM`
						`alpha_k_polSM`
						`alpha_k_torSM`
	Max var dir in GSE	deg	eigenvector $\boldsymbol{v}'_1$	(10)	McPherron et al. (1972)	`maxvar_theta_gse`
						`maxvar_phi_gse`
n	PSD of n	$\mathrm{cm^{-6}\,Hz^{-1}}$	$2W\lvert\tilde{n}\rvert^2$			`dens_psd`
$\boldsymbol{E}$	Total PSD of $\boldsymbol{E}$	$\mathrm{mV^2\,m^{-2}\,Hz^{-1}}$	$2W\operatorname{Tr}(\mathcal{S}^E)$			`E_spec_total`

Table S2. Parameters derived from multiple quantities

input	parameter	unit	expression	Eq.	file name
$\boldsymbol{B}$,$\boldsymbol{E}$	Poynting vector components in GSE	$\mathrm{mW\,km^{-2}\,Hz^{-1}}$	$2W\Re(\tilde{\boldsymbol{E}} \times \tilde{\boldsymbol{B}}^{\star})/(2\mu_0)$	(23)	`ptg_xGSE`
					`ptg_yGSE`
					`ptg_zGSE`
	Poynting vector direction in GSE	deg			`ptg_theta_gse`
					`ptg_phi_gse`
	Poynting vector magnitude	$\mathrm{mW\,km^{-2}\,Hz^{-1}}$			`ptg_module`
	Poynting vector components in MFA	$\mathrm{mW\,km^{-2}\,Hz^{-1}}$			`ptg_parallelMFA`
					`ptg_azimuthalMFA`
					`ptg_radialMFA`
	Poynting vector – LMC axes angles	deg	$\arccos(S_{j\mathrm{LMC}}/\lvert\boldsymbol{S}\rvert)$		`alpha_ptg_radSM`
					`alpha_ptg_polSM`
					`alpha_ptg_torSM`
	Poynting vector – magnetic field angle	deg	$\arccos(\boldsymbol{S} \cdot \langle\boldsymbol{B}\rangle)$		`sb_angle`
	Poynting vector – wave vector angle	deg	$\arccos(\boldsymbol{S} \cdot \boldsymbol{k})$		`sk_angle`
$\lvert\boldsymbol{B}\rvert$,$n$	Magnetic field – density coherence	–	$\lvert\mathcal{G}_{Bn}\rvert/(\mathcal{G}_{BB}\mathcal{G}_{nn})$	(22)	`bd_coh`
	Magnetic field – density phase	deg	$\arg(\mathcal{G}_{Bn})$	(21)	`bd_phase`
	Magnetic field – density co-spectrum	$\mathrm{cm^{-3}\,nT\,Hz^{-1}}$	$2W\lvert\Re(\mathcal{G}_{Bn})\rvert$	(20)	`bd_cosp`
	Magnetic field – density quad-spectrum	$\mathrm{cm^{-3}\,nT\,Hz^{-1}}$	$2W\lvert\Im(\mathcal{G}_{Bn})\rvert$		`bd_quadsp`

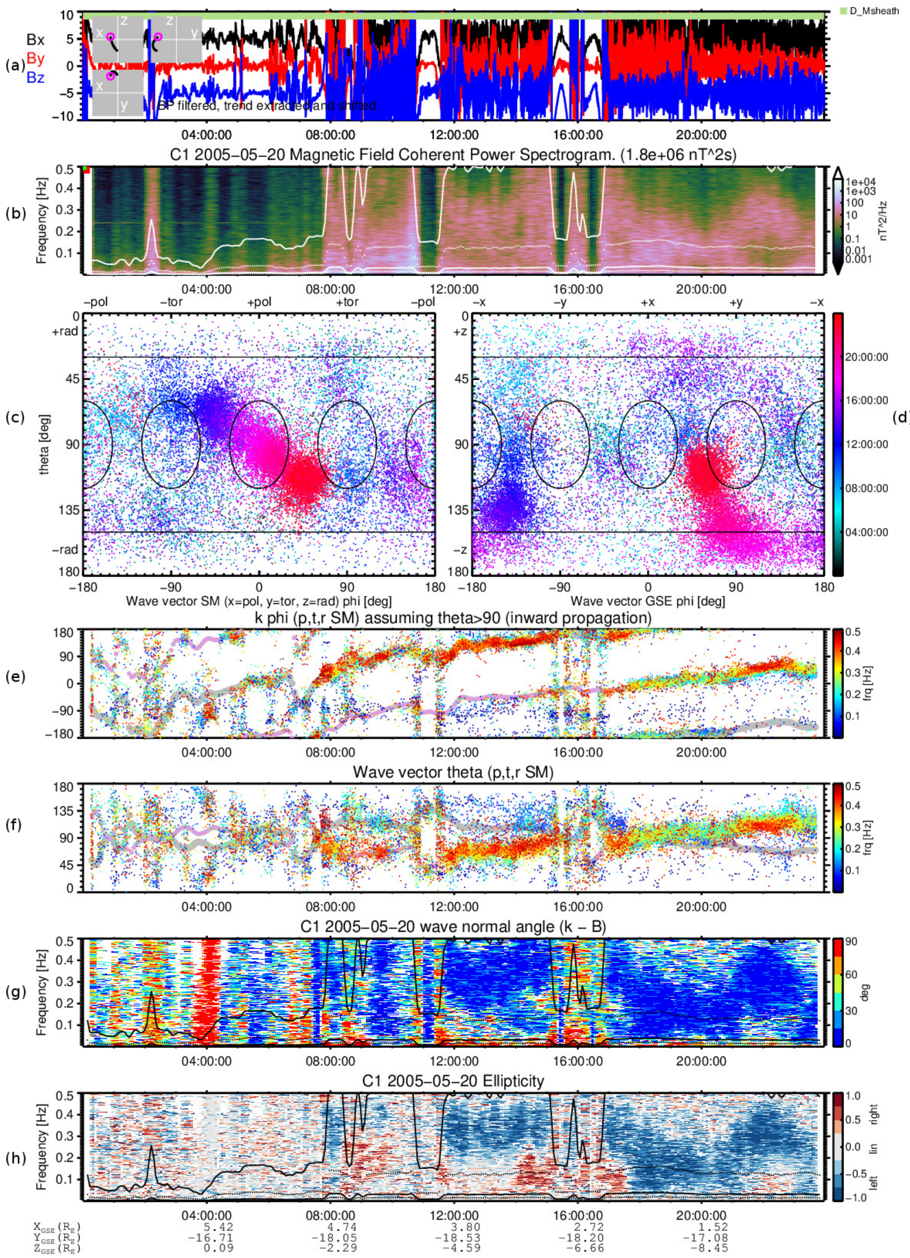

Figure S1. The *wave vector direction* plot set for Cluster 1 on 20th May 2005. The top panel (a) and the bottom two panels (g,h) are the same as in Fig. 1. Panel (b) shows the PSD of the coherent part of the magnetic field. The next two panels show the wave vector orientation in the LMC system (c) and in GSE (d). The two panels below (e,f) show the wave vector orientation in the LMC system. The mean magnetic field direction is plotted with the thick grey line. The magenta line shows the direction anti-parallel to the mean magnetic field.

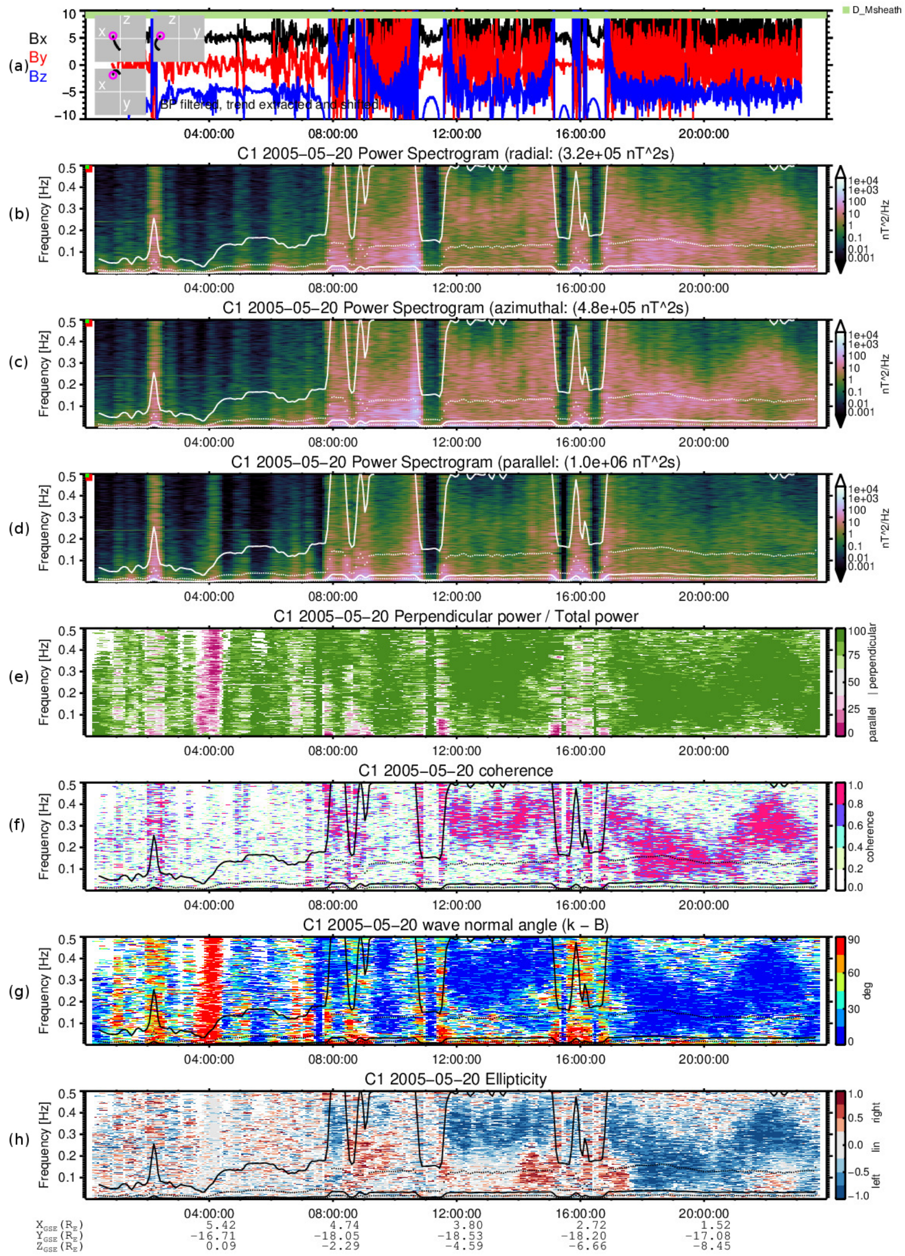

Figure S2. The *B MFA* plot set for Cluster 1 on 20th May 2005. The top panel (a) is similar to the top panel in Fig. 1. The three panels below (b,c,d) show the PSD of the magnetic field in the MFA system, separated on components. Panel (e) shows the ratio between the power of the oscillations in the orthogonal direction to the magnetic field and the total wave power. Panel (f) shows the coherency. The last two panels (g,h) are the same as in Fig. 1.

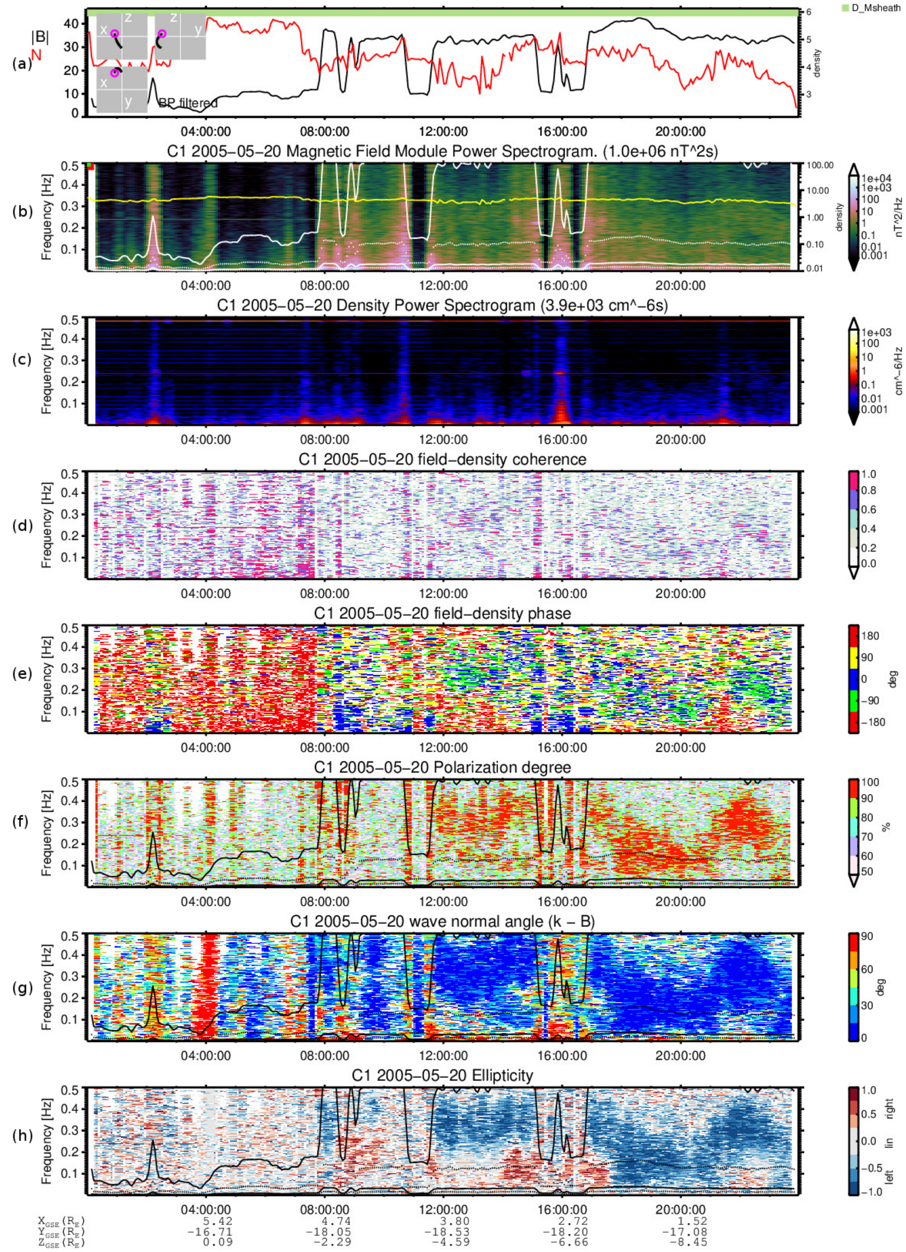

Figure S3. The *B - density* plot set for Cluster 1 on 20th May 2005. Panel (a) shows the magnitude of the magnetic field (black) and the plasma density (red), both smoothed with a 512 s window; Panel (b) shows the PSD of the magnetic field magnitude with the electron density over-plotted with yellow; Panel (c) shows the PSD of the density fluctuations; Panel (d) shows the coherency between the magnetic field and the plasma density fluctuations; Panel (e) shows the phase difference between the magnetic field magnitude and the density fluctuations. Panels (f,g,h) are the same as in Fig. 1.

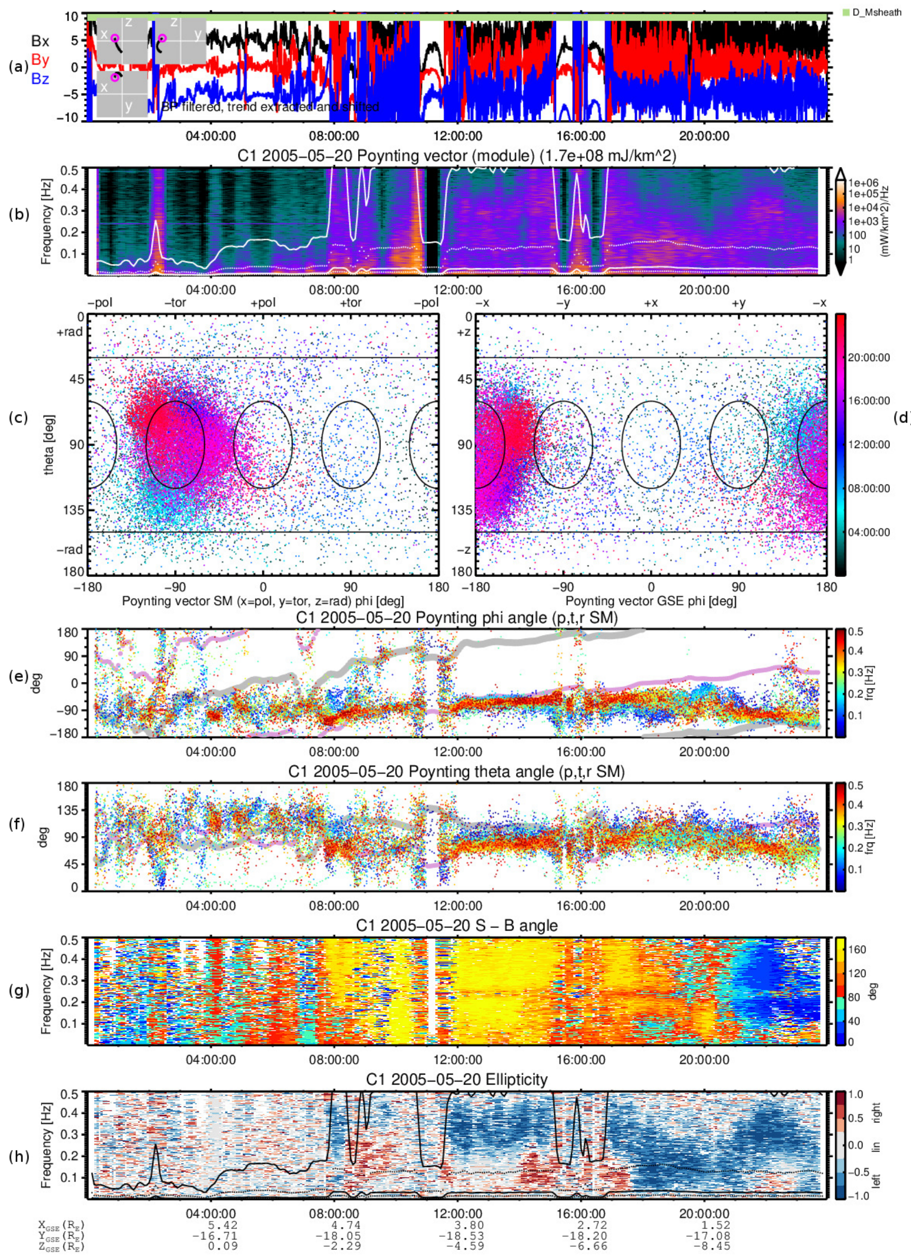

Figure S4. The *Poynting vector direction* plot set for Cluster 1 on 20th May 2005. The top and bottom panels (a,h) are same as in Fig. 1. Panel (b) shows the PSD of the Poynting vector magnitude and the gyrofrequencies of H, He, O, and O_2. Panels (c,d) are similar with those in Fig. S1 but instead of the wave vector direction show the Poynting vector direction. Panels (e,f) show the Poynting vector direction in the LMC system. Panel (g) shows the angle between the Poynting vector and the mean magnetic field.

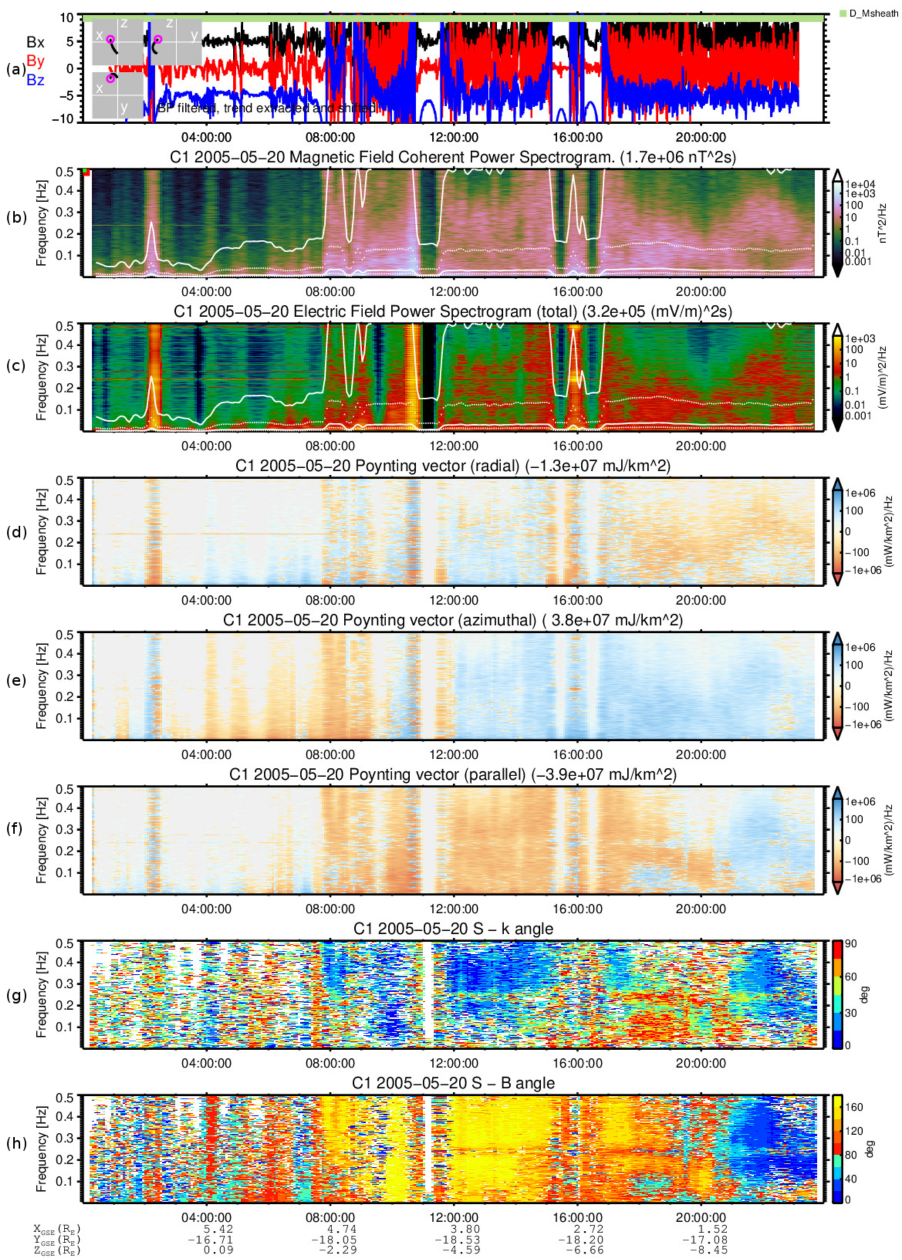

Figure S5. The *Poynting vector MFA* plot set for Cluster 1 on 20th May 2005. From top to bottom: (a) The magnetic field in MFA system; (b) the PSD of the coherent part of magnetic field fluctuations; (c) The sum of the PSD of the electric field components; (d,e,f) The radial, azimuthal, and parallel components of the Poynting vector in the MFA system; (g) The angle between the Poynting vector and the wave vector; (h) The angle between the Poynting vector and the mean magnetic field.

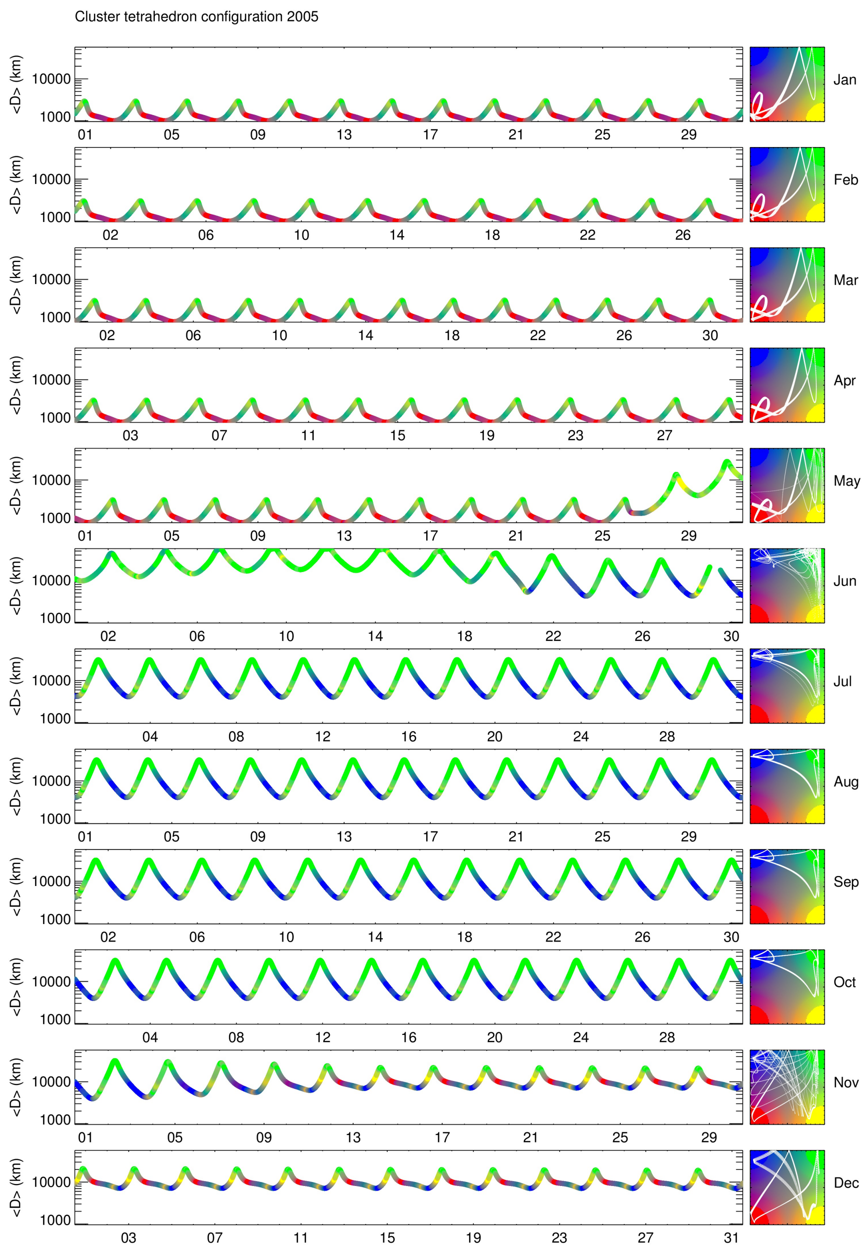

Figure S6. Yearly overview of the mean separation and tetrahedron shape for 2005. The tetrahedron shape is colour coded and the trajectories in the (e,p) domain are plotted with white in the colour-keys for each month.

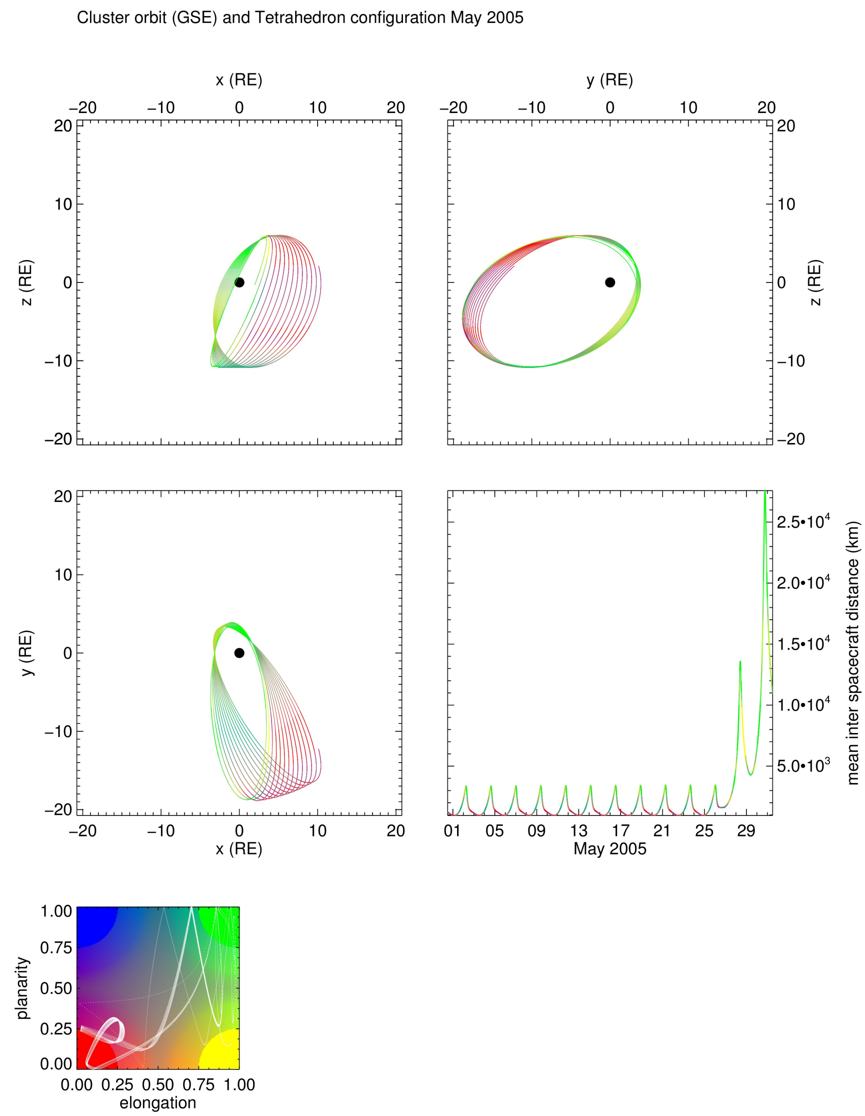

Figure S7. Orbit and configuration parameters of the Cluster tetrahedron during May 2005. The orbits of the formation barycentre are plotted in GSE coordinates and colour coded for the shape with the colour-key in the lower left. The trajectory in the (e,p) plane is shown in white in the colour-key.

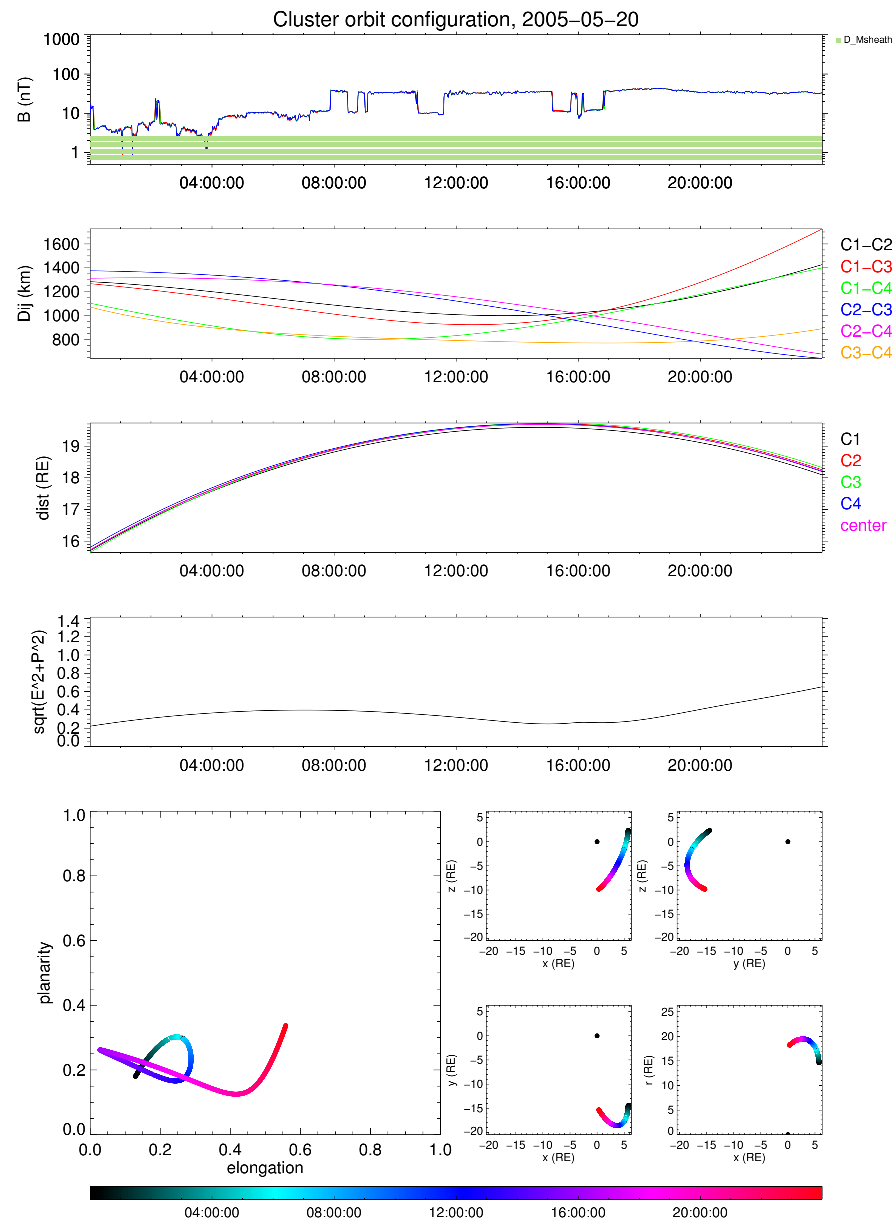

Figure S8. Daily plot for 20th May 2005. From top to bottom: Magnetic field magnitude for the four spacecraft and the magnetospheric regions from SSCWeb. Inter-spacecraft distances. Radial distances for the spacecraft and for the formation barycentre. Degeneration degree of the tetrahedron. The bottom left plot: trajectory in the (e,p) domain, colour codes the time. The four bottom right plots: barycentre orbit in GSE and barycentre radial distance.

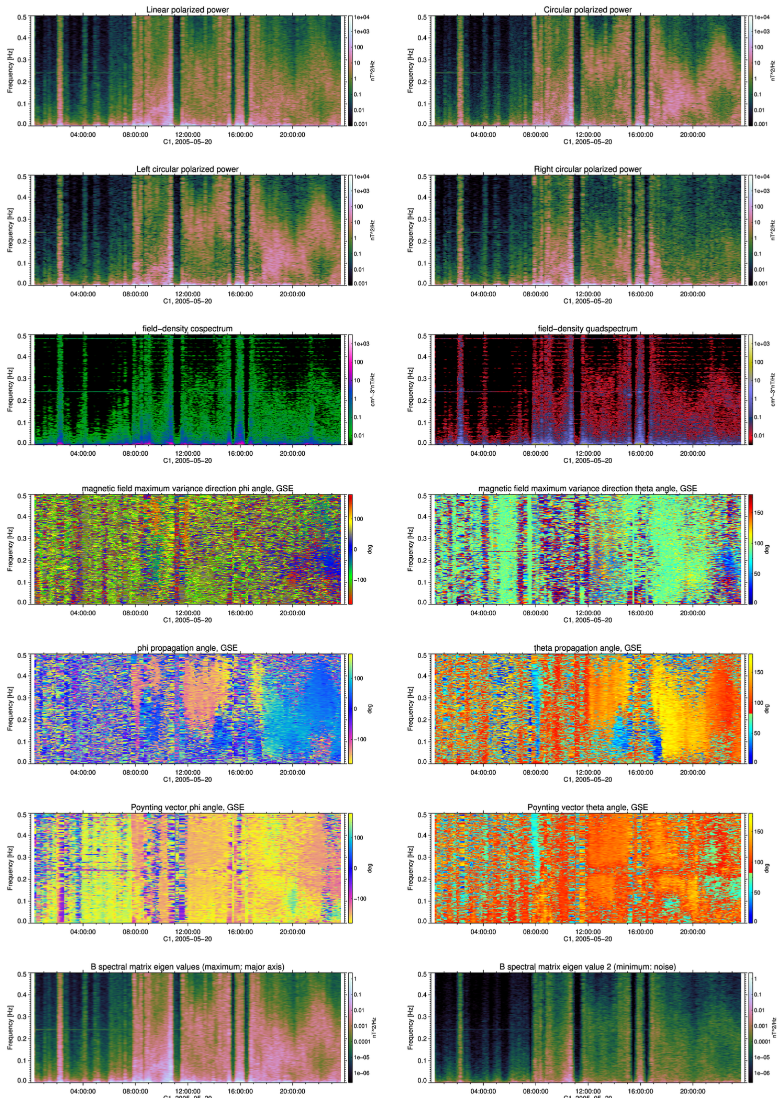

Figure S9. Subset of low resolution quick-view plots for the HDF data archive. No masks are applied. The first panel shows the power spectral density of the linear polarized part of the waves, $\rho_{\rm lin} = 2WA^2_{\rm lin}$, with the amplitude of the linear part, $A_{\rm lin}$ from Eq. (17). The PSD of the circular polarized part of the waves is shown next. The circular polarized waves are further divided into the left $\rho_{\rm left} = 2WA^2_-$ and the right $\rho_{\rm right} = 2WA^2_+$ polarization in the following two panels. The co- and quadspectrum of the magnetic field - density fluctuations are shown in the next row. The following three rows show the directions of the magnetic field maximum variance, wave propagation direction, and Poynting vector in GSE coordinates. The last two panels show the maximum and the minimum eigenvalues of the magnetic field spectral matrix.

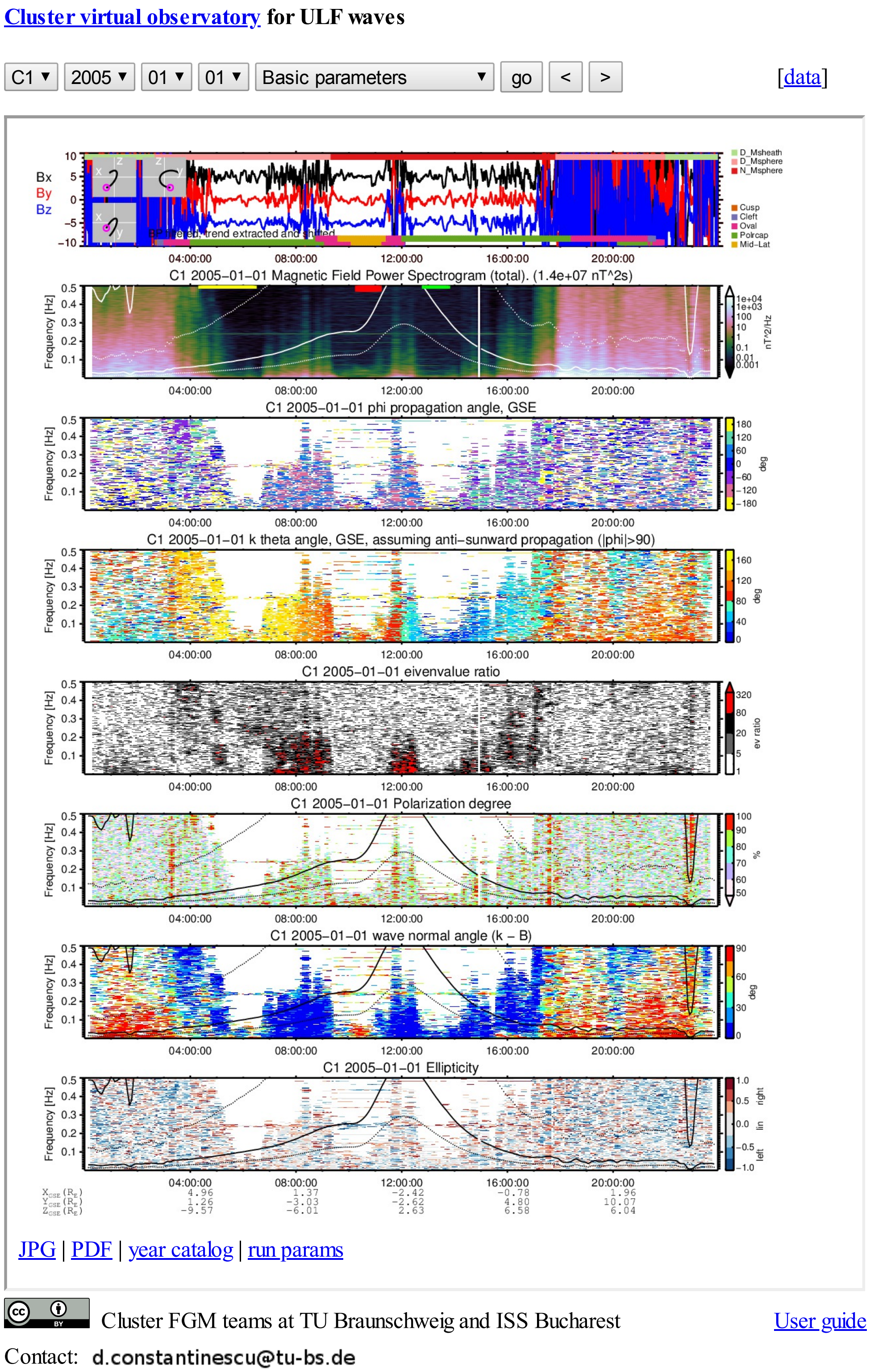

Figure S10. The plots section of the CVO.

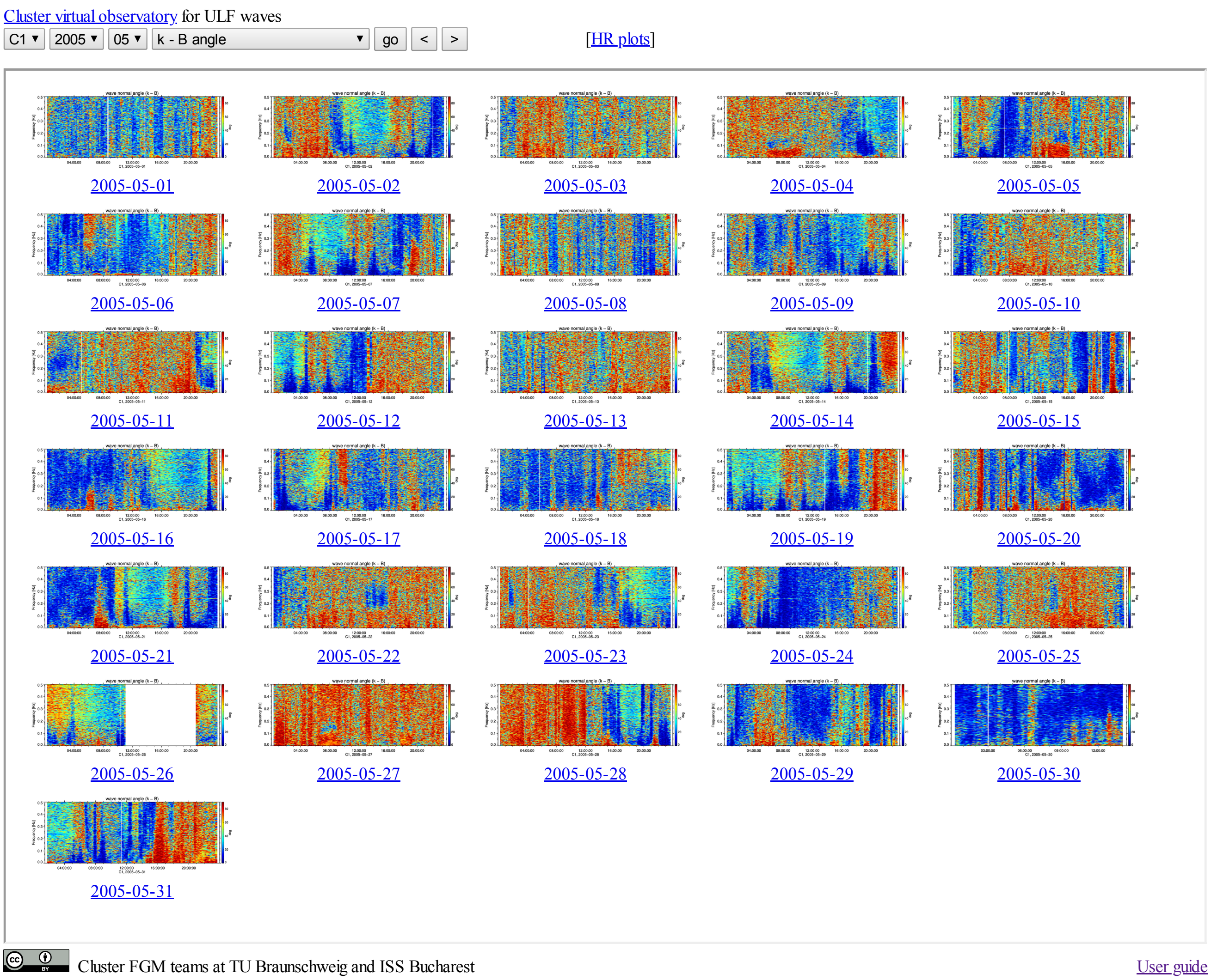

Figure S11. The data section of the CVO.

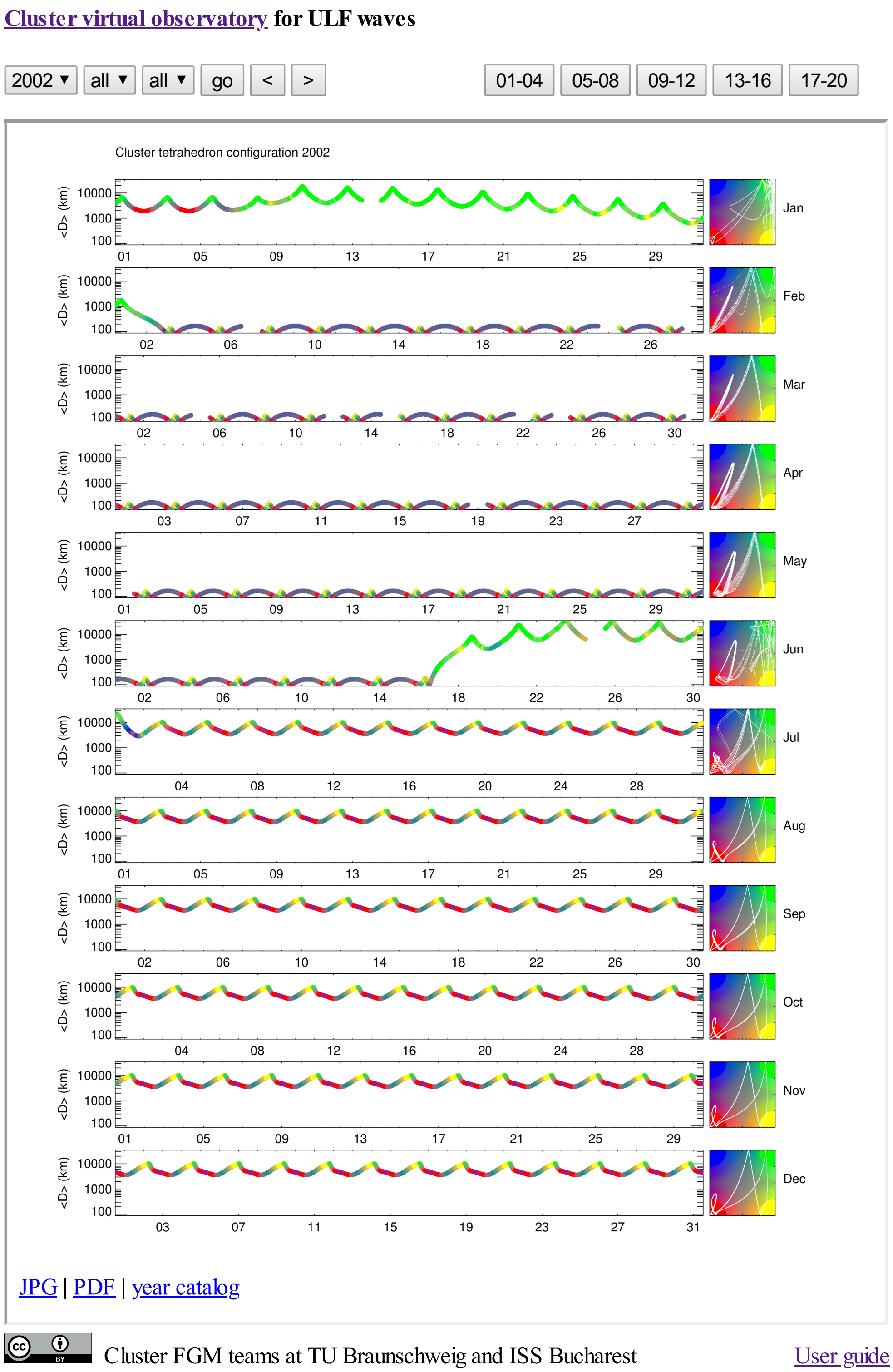

Figure S12. The tetrahedron configuration section of the CVO.